

2022-02-15

Geometric asymmetry in the energy conversion and wave attenuation of a power-take-off-integrated floating breakwater

Zhou, B

<http://hdl.handle.net/10026.1/18597>

10.1016/j.oceaneng.2022.110576

Ocean Engineering

Elsevier

All content in PEARL is protected by copyright law. Author manuscripts are made available in accordance with publisher policies. Please cite only the published version using the details provided on the item record or document. In the absence of an open licence (e.g. Creative Commons), permissions for further reuse of content should be sought from the publisher or author.

Title:

Geometric asymmetry in the energy conversion and wave attenuation of a power-take-off-integrated floating breakwater

Journal:

Ocean Engineering

Author names and affiliations:

Binzhen Zhou^a, Qi Zhang^b, Peng Jin^{c,*}, Yan Li^{d,e}, Yingyi Liu^f, Siming Zheng^g, Dezhi Ning^h

^a School of Civil Engineering and Transportation, South China University of Technology, Guangzhou 510641, China

^b College of Shipbuilding Engineering, Harbin Engineering University, Harbin 150001, China

^c School of Marine Science and Engineering, South China University of Technology, Guangzhou 510641, China

^d Department of Energy and Process Engineering, Norwegian University of Science and Technology, N-7491 Trondheim, Norway

^e Department of Engineering Science, University of Oxford, Parks Road, Oxford OX1 3PJ, UK

^f Research Institute for Applied Mechanics, Kyushu University, Kasuga 816-8580, Japan

^g School of Engineering, Computing and Mathematics, University of Plymouth, Drake Circus, Plymouth PL4 8AA, United Kingdom

^h State Key Laboratory of Coastal and Offshore Engineering, Dalian University of Technology, Dalian, 116024, China

doi: 10.1016/j.oceaneng.2022.110576

Received 12 December 2021, Accepted 6 January 2022, Available online 20 January 2022.

* Corresponding author

E-mail address: jinpeng@scut.edu.cn (P. Jin)

Geometric asymmetry in the energy conversion and wave attenuation of a power-take-off-integrated floating breakwater

Binzhen Zhou^a, Qi Zhang^b, Peng Jin^{c,*}, Yan Li^{d,e}, Yingyi Liu^f, Siming Zheng^g, Dezhi Ning^h

^a School of Civil Engineering and Transportation, South China University of Technology, Guangzhou 510641, China

^b College of Shipbuilding Engineering, Harbin Engineering University, Harbin 150001, China

^c School of Marine Science and Engineering, South China University of Technology, Guangzhou 510641, China

^d Department of Energy and Process Engineering, Norwegian University of Science and Technology, N-7491 Trondheim, Norway

^e Department of Engineering Science, University of Oxford, Parks Road, Oxford OX1 3PJ, UK

^f Research Institute for Applied Mechanics, Kyushu University, Kasuga 816-8580, Japan

^g School of Engineering, Computing and Mathematics, University of Plymouth, Drake Circus, Plymouth PL4 8AA, United Kingdom

^h State Key Laboratory of Coastal and Offshore Engineering, Dalian University of Technology, Dalian, 116024, China

Abstract

A hybrid system integrating a power take-off (PTO) system into a floating breakwater is a promising candidate for both shoreline protection and commercial wave energy extraction. Although geometric asymmetry is important to such PTO-integrated breakwaters, its role in energy conversion efficiency and wave attenuation is poorly understood. In this study, a two-dimensional semi-analytical model dealing with floats with arbitrary bottom shapes is established based on the potential flow theory. To quantify the geometric asymmetry reflected by PTO-integrated breakwaters with different contours, the degree of asymmetry and the absolute asymmetry are newly defined mathematically. A set of symmetric and asymmetric PTO-integrated breakwaters are comparatively studied to demonstrate the effect of linear PTO damping and geometric asymmetry on the transmission coefficient, the reflection coefficient, and the energy conversion efficiency. Results show that no matter the hybrid system is symmetric or asymmetric, a larger PTO damping is beneficial for wave attenuation in longer waves, particularly at the heaving natural period of the device. On the premise that the PTO damping is optimized, an increase in the degree of asymmetry greatly improves the energy conversion efficiency. An increase in the absolute asymmetry slightly improves wave attenuation.

Keyword: Breakwater; Wave energy converter; Hybrid system; Geometric asymmetry; Energy conversion efficiency; Wave attenuation

* Corresponding author

E-mail address: jinpeng@scut.edu.cn (P. Jin)

1. Introduction

The extensive and commercial exploitation of wave energy is hindered by the high manufacturing and installation cost of WECs. A practical solution is to incorporate WECs in available oceanic or coastal infrastructures to form an integrated system [1]-[5], wherein the infrastructures provide an installation foundation for the WECs. The integration of WECs and breakwaters is beneficial from their cost-sharing and compatible functions of energy extraction and shoreline protection. Due to the variety of WECs [6] and breakwaters [7], the layout of a hybrid system is quite diverse [8]-[10]. Two methods are usually adopted while incorporating an oscillating body WEC: 1) the WEC is deployed as a separated unit on the seaward side of the breakwater, such as in Zhang et al. [11], Reabroy et al. [12], and Zhang et al. [13]. 2) the floating breakwater is used as the oscillating component and the power take-off (PTO) system is integrated in it (PTO-integrated breakwater hereafter), for instance in Zhang et al. [14] and Ning et al. [15].

The studies of PTO-integrated breakwaters could roughly be categorized into two aspects according to the subject. In the first, the subject is a standard rectangular float. Investigations are mainly on the influence of geometric factors and generator parameters on the hydrodynamic and power performance. Ning et al. [15] conducted experiment on a wave tank to study the effect of incident wave conditions, PTO damping, and dimensions of the breakwater on energy conversion efficiency and wave attenuation. They found that the PTO damping force and the draft and width of the breakwater play important roles in the hydrodynamic performance. Using Open-Foam, Ma et al. [16] extended the work of Ning et al. [15] to study the performance of three kinds of integrated PTO and found that applying Coulomb damping is suitable for wave energy capturing and coastal protection. Zhao et al. [17] took an experiment to study the influence of PTO damping on the wave loads acting on different areas of the float. They found that the wave pressure on the front and back walls is seriously affected, whereas the wave pressure on the middle section of the bottom is the smallest and just slightly affected by the PTO damping force.

In the second, the subject is no longer a standard rectangular float. Either the number of floats is increased or the cross-section of a single-float is modified as new concepts. Investigations are still on the influence of different factors on the performance of the system. Using the Computational Fluid Dynamics (CFD) approach, Chen et al. [18] studied a PTO-integrated breakwater in which a permanent magnet linear generator is installed inside a sealed floating horizontal circular cylindrical buoy. Its maximum primary energy conversion efficiency could be close to 25% with a corresponding wave transmission coefficient ranging from 0.7 to 0.75. Ning et al. [19] extended their work in Ning et al. [15] and proposed a dual float design. They studied the influence of the geometric parameters of the system and found that the heaving natural frequency and the spacing between the two floats are critical factors to its performance. The bandwidth of energy conversion in the frequency domain is also broader compared with a single float. Guo et al. [20] further extended the work and proposed a triple float design that can absorb wave energy from both heave and pitch motions. They studied the influence of the width and draft of the floats and the spacing between the floats and found that the effective energy conversion bandwidth increases with the decrease of the width and draft of the front float, and the spacing also plays an important role. Based on potential flow theory with viscous correction in the frequency domain, Zhang et al. [21] design and optimize a three-dimensional

1 floating breakwater integrated with a WEC array, and find that the WECs perform better when
2 it is placed in the wave focusing areas, which appear more frequently close to the breakwater.
3 The vertical forces on the breakwater significantly increase and the horizontal forces are
4 decreased.

5 Since Mei [22] indicated that the efficiency of a symmetric WEC could not exceed 50%,
6 some subsequent concepts using an asymmetric float instead of a symmetric float have been
7 proposed and studied. Perhaps the first such device being propounded is the “Berkeley Wedge”.
8 Based on the idea that the WEC should 1) be highly asymmetric to overcome the efficiency
9 limit of 50% and 2) minimize the impediment of viscosity, the odd shape of Berkeley Wedge
10 was obtained. The Berkeley Wedge WEC was later used as a PTO-integrated breakwater [23].
11 Zhang et al. [14] studied the energy conversion efficiency and wave attenuation of three
12 asymmetric PTO-integrated breakwaters with different bottom configurations and found that a
13 simple triangle-baffle model is as efficient as the Berkeley Wedge. The efficiency could be up
14 to 93%. Chen et al. [24] used a Particle in Cell (PIC) numerical scheme to optimize the cross-
15 section of a PTO-integrated breakwater for more energy absorption and less wave transmission
16 at the same time. They found that using a small circular arc corner instead of a rectangular
17 corner on the seaward side greatly improves the energy conversion efficiency with a slight
18 decline in wave attenuation.

19 From the literature, it is consensual that asymmetry has a significant influence on the energy
20 conversion efficiency and wave attenuation of a PTO-integrated breakwater. Although previous
21 research has taken efforts in optimizing the standard rectangular float or proposing new designs
22 based on this idea, the way the performance is influenced by asymmetry and corresponding
23 mechanisms are somewhat overlooked. To fill this gap, a theoretical investigation was
24 performed. The novelties of this study are as follows: 1) to propose and validate a semi-
25 analytical approach based on the eigenfunction expansion method dealing with floats with
26 arbitrary bottom shapes; 2) to introduce the concepts of the degree of asymmetry and the
27 absolute asymmetry and establish criteria for qualifying and comparing such property between
28 different PTO-integrated breakwaters; 3) to investigate the role of asymmetry in the
29 proportional distribution of attenuated, reflected, and absorbed wave energy; 4) to study the
30 effect of three approaches that can modify the asymmetry of a triangular-wedge PTO-integrated
31 breakwater on its energy conversion efficiency and wave attenuation, providing a useful
32 reference for practical design and application.

33 The rest of the paper is structured as follows. In Section 2, the mathematical model describing
34 interactions between waves and a PTO-integrated breakwater with arbitrary bottom shape is
35 given. Only the major steps are displayed in this part whereas the detailed expressions of some
36 terms are given in the Appendices for readers to capture the essence conveniently. In Section 3,
37 convergence tests on bottom shape asymptote are conducted, and a comparison of results with
38 a widely used numerical schematic is performed to validate the present model. A comparative
39 study using a wide range of PTO damping on three symmetric and asymmetric PTO-integrated
40 breakwaters is done to check if installing a PTO system could improve its wave attenuation.
41 The role of geometric asymmetry in energy conversion efficiency and wave attenuation is
42 investigated in detail. In Section 4, three approaches to change the geometric asymmetry of a
43 triangular-wedge PTO-integrated breakwater are examined. Their influence on the performance
44 of the breakwater is investigated. In Section 5, conclusions are drawn.

1

2

3
4
5
6
7
8
9
10
11

12
13
14
15
16
17



20

21
22
23
24
25
26
27
28
29
30

31

$$\gamma_1 = d_A/w^B \quad (2)$$

$$\gamma_2 = (V_A^{\text{lee}} - V_A^{\text{sea}})/(V_A^{\text{lee}} + V_A^{\text{sea}}) \quad (3)$$

where w^B is the width of the structure. If $V_A^{\text{lee}} + V_A^{\text{sea}} \neq 0$ and $V_A^{\text{lee}} + V_A^{\text{sea}} = 0$, $\gamma_2 = 0$. This definition reveals that the DoA is a combination of two aspects: 1) γ_1 is the ratio of the draft to the width of the asymmetric part, reflecting the influence of the horizontal dimension; 2) γ_2 is the ratio of the difference between the displacement of the leeward part and the seaward part to the total displacement of the asymmetric part, reflecting the inequality between the two components on the two sides of the central line. Straightforwardly, $|\gamma|$ is the absolute asymmetry of the structure. Note that the draft of a breakwater has a great influence on its wave attenuation [14]. The application of DoA and absolute asymmetry should be limited in the comparison between two structures with the same draft, otherwise, the comparison may be meaningless. When $\gamma < 0$, the displacement of the PTO-integrated breakwater mainly concentrates on the seaward side; when $\gamma = 0$, the structure could be symmetric and could be asymmetric with bottom displacement $V_A^{\text{sea}}=V_A^{\text{lee}}$, which is complex with too many parameters and not included in the study; when $\gamma > 0$, the displacement mainly concentrates on the lee side.

2.2. Governing equation and boundary conditions

The float is subjected to a regular wave train with an angular frequency ω traveling in the positive x -direction. In the framework of linear potential flow theory, the water flow could be described by the velocity potential

$$\phi(x, z, t) = \text{Re}[\varphi(x, z)e^{-i\omega t}], \quad (4)$$

where $i = \sqrt{-1}$ is the imaginary unit and t denotes time. $\varphi(x, z)$ is the time-independent complex spatial velocity potential that satisfies Laplace's equation,

$$\partial_{xx}\varphi + \partial_{zz}\varphi = 0. \quad (5)$$

φ could be decomposed into scattering and radiation potentials, i.e., $\varphi = \varphi_0 - i\omega\xi_3\varphi_3$. The scattering potential φ_0 is the sum of the incident potential φ^I and the diffraction potential φ^D . ξ_3 is the amplitude of response heave motion. φ_3 is the radiation potential due to heave motion of the float with unit velocity. φ satisfies the following linearized boundary conditions,

$$g\partial_z\varphi = \omega^2\varphi, \text{ on the free surface } z = 0, \quad (6)$$

$$\partial_z\varphi = 0, \text{ on the seabed } z = -h, \quad (7)$$

$$\partial_n\varphi_3 = n_3, \text{ on the fluid and float interface}, \quad (8)$$

$$\varphi^D, \varphi_3 \text{ outgoing; finite value, in the far-field } |x| \rightarrow \infty, \quad (9)$$

where g is the acceleration of gravity, \vec{n} is the unit normal vector on the fluid and float interface, directed into the float, and n_3 is the component of unit normal vector \vec{n} in the heave mode.

2.3. Explicit expressions for potentials

The incident velocity potential could be easily expressed following [25],

$$\varphi^I = -\frac{igA \cosh[k_0(z+h)]}{\omega \cosh(k_0 h)} e^{ik_0(x-x_0)}. \quad (10)$$

where A is the wave amplitude, k_0 is the wavenumber of propagating waves, obeying the dispersion relation $\omega^2 = gk_0 \tanh(k_0 h)$. Based on Eqs. (5)-(9) and using the separation of variables, the velocity potential in each subdomain could be given according to [22] and [26].

1 For $i = 1, \dots, N$ and $j = 0, 3$,

$$2 \quad \varphi_j^{\Omega_0} = \delta_{0j} \varphi^I + \left(-\frac{igA}{\omega}\right)^{\delta_{0j}} \left[\begin{array}{c} R_{0j}^{\Omega_0} e^{-ik_0(x-x_0)} Z_0(z) + \\ \sum_{m=1}^{\infty} R_{mj}^{\Omega_0} e^{k_m(x-x_0)} Z_m(z) \end{array} \right], \quad (11)$$

$$3 \quad \varphi_j^{\Omega_i} = \left(-\frac{igA}{\omega}\right)^{\delta_{0j}} \left[\begin{array}{c} \varphi_j^{p,\Omega_i} + (S_{0j}^{\Omega_i} + T_{0j}^{\Omega_i} x) Y_0^{\Omega_i}(z) + \\ \sum_{l=1}^{\infty} (S_{lj}^{\Omega_i} e^{\lambda_l^{\Omega_i} x} + T_{lj}^{\Omega_i} e^{-\lambda_l^{\Omega_i} x}) Y_l^{\Omega_i}(z) \end{array} \right], \quad (12)$$

$$4 \quad \varphi_j^{\Omega_{N+1}} = \left(-\frac{igA}{\omega}\right)^{\delta_{0j}} \left[R_{0j}^{\Omega_{N+1}} e^{ik_0(x-x_N)} Z_0(z) + \sum_{m=1}^{\infty} R_{mj}^{\Omega_{N+1}} e^{-k_m(x-x_N)} Z_m(z) \right], \quad (13)$$

5 where δ is the Kronecker Delta function. $\delta = 1$ when the two indices in the subscript are
6 equal and $\delta = 0$ otherwise. $R_{0j}^{\Omega_0}$, $R_{mj}^{\Omega_0}$, $S_{0j}^{\Omega_i}$, $S_{lj}^{\Omega_i}$, $T_{0j}^{\Omega_i}$, $T_{lj}^{\Omega_i}$, $R_{0j}^{\Omega_{N+1}}$, and $R_{mj}^{\Omega_{N+1}}$ ($m, l =$
7 $1, 2, \dots$) are unknown coefficients to be determined. In Ω_0 and Ω_{N+1} , k_m ($m = 1, 2, \dots$) is the
8 wavenumber of evanescent waves, obeying the dispersion relation $\omega^2 = -gk_m \tan(k_m h)$
9 [27]. The corresponding eigenfunctions $Z_0(z)$ and $Z_m(z)$ are defined by

$$10 \quad Z_0(z) = \frac{\cosh[k_0(z+h)]}{\cosh(k_0 h)}, \quad Z_m(z) = \frac{\cos[k_m(z+h)]}{\cos(k_m h)}. \quad (14)$$

11 $\lambda_0^{\Omega_i}$ and $\lambda_l^{\Omega_i}$ ($l = 1, 2, \dots$) are the eigenvalues in the subdomains Ω_i . Subjected to the
12 homogeneous boundary conditions on the seabed (Eq. (7)) and the bottom of the asymptotic
13 float while it is static,

$$14 \quad \partial_z \varphi = 0, \text{ on the bottom of the asymptotic float } z = -d_i, \quad (15)$$

15 $\lambda_0^{\Omega_i} = 0$ and $\lambda_l^{\Omega_i} = l\pi/(h - d_i)$. The corresponding eigenfunctions $Y_0^{\Omega_i}(z)$ and $Y_l^{\Omega_i}(z)$ are
16 given by

$$17 \quad Y_0^{\Omega_i}(z) = \frac{\sqrt{2}}{2}, \quad Y_l^{\Omega_i}(z) = \cos[\lambda_l^{\Omega_i}(z + h)]. \quad (16)$$

18 φ_j^{p,Ω_i} is a solution of radiation potential in Ω_i satisfying the non-homogeneous condition in
19 Eq. (8). Based on [22] and [26], it could be expressed as

$$20 \quad \varphi_j^{p,\Omega_i} = \frac{(z+h)^2 - x^2}{2(h-d_i)} \delta_{3j}. \quad (17)$$

21 2.4. Continuity conditions

22 To solve the unknown coefficients in Eqs. (11)-(13), three types of continuity conditions on
23 the interface between each pair of adjacent subdomains at $x = x_i$, $i = 0, \dots, N$, are required.
24 Let \hat{i} denotes the index of $\max(-d_i, -d_{i+1})$, \check{i} denotes the index of $\min(-d_i, -d_{i+1})$.
25 For $j = 0, 3$, the conditions are as follows:

26 1) Continuity of velocity potential on the fluid interface $x = x_i$, $-h < z < -d_{\hat{i}}$:

$$27 \quad \varphi_j^{\Omega_{\hat{i}}} = \varphi_j^{\Omega_{\check{i}}}. \quad (18)$$

28 2) Continuity of horizontal velocity on the fluid interface $x = x_i$, $-h < z < -d_{\hat{i}}$:

$$29 \quad \partial_x \varphi_j^{\Omega_{\hat{i}}} = \partial_x \varphi_j^{\Omega_{\check{i}}}. \quad (19)$$

30 3) Continuity of horizontal velocity on the solid boundary $x = x_i$, $-d_{\check{i}} < z < -d_{\hat{i}}$:

$$31 \quad \partial_x \varphi_j^{\Omega_{\check{i}}} = 0. \quad (20)$$

For simplicity, use $\text{eigen}_i(z)$ to represent the eigenfunction in the i th subdomain. Thus $\text{eigen}_0(z) = \text{eigen}_{N+1}(z) = Z_m(z)$. In Ω_i , $\text{eigen}_i(z) = Y_l^{\Omega_i}(z)$, $i = 1, \dots, N$. To make the equation system a complete set to solve the unknowns coefficients in Eqs. (11)-(13), the velocity potential and velocity terms in Eqs. (18)-(20) need to be multiplied by eigenfunctions and then integrated over the interfaces, i.e., for $i = 0, \dots, N+1$, the integral for Eq. (18) is

$$\int_{-h}^{-d_i} \varphi_j^{\Omega_i} \text{eigen}_i(z) dz = \int_{-h}^{-d_i} \varphi_j^{\Omega_i} \text{eigen}_i(z) dz, \quad (21)$$

and the integral for Eq. (19) and (20) is

$$\int_{-h}^{-d_i} \partial_x \varphi_j^{\Omega_i} \text{eigen}_i(z) dz = \int_{-h}^{-d_i} \partial_x \varphi_j^{\Omega_i} \text{eigen}_i(z) dz. \quad (22)$$

Substituting the expressions for φ_j in Eqs. (11)-(13) into Eqs. (21)-(22) and truncating the first M terms in $R_{mj}^{\Omega_0}$ and $R_{mj}^{\Omega_{N+1}}$ and the first L terms in $S_{lj}^{\Omega_i}$ and $T_{lj}^{\Omega_i}$ yield a linear system of $2(M+1) + 2N(L+1)$ complex Eqs for each j .

$$\mathbf{A}\mathbf{X}_j = \mathbf{B}_j \quad (23)$$

where $\mathbf{X}_j = [R_{0j}^{\Omega_0}, \dots, R_{Mj}^{\Omega_0}, S_{0j}^{\Omega_1}, \dots, S_{Lj}^{\Omega_1}, T_{0j}^{\Omega_1}, \dots, T_{Lj}^{\Omega_1}, R_{0j}^{\Omega_{N+1}}, \dots, R_{Mj}^{\Omega_{N+1}}]^T$. \mathbf{A} is the coefficient matrix, which is determined by the shape of the float. The expressions of \mathbf{A} and \mathbf{B}_j are given in Appendix.

2.5. Wave excitation force, added mass, and radiation damping

The wave excitation forces in the heave could be computed by summing the components in each subdomain,

$$F_k^{\text{EX}} = i\omega\rho \sum_{i=0}^{N+1} \int_{\Omega_i} \varphi_0(x, z) n_3 ds, \quad (24)$$

where ρ is the density of water.

The radiation force in the k th mode due to the motion in the heave mode could be computed by summing the components in each subdomain,

$$F_k^{\text{R}} = v_3 f_{k3}^{\text{R}} \text{ with } f_{k3}^{\text{R}} = i\rho\omega \sum_{i=0}^{N+1} \int_{\Omega_i} \varphi_3 n_k ds, \quad (25)$$

where v_3 is the velocity of the float in the heave mode. By some manipulation [22],

$$F_k^{\text{R}} = -a_{k3} \dot{v}_3 + b_{k3} v_3. \quad (26)$$

The dot above v_3 denotes the derivative to t . Denote a_{k3} as the added mass and b_{k3} as the radiation damping in the k th mode due to the motion in the heave mode which can be written as:

$$a_{k3} = \frac{1}{\omega} \text{Im}[f_{k3}^{\text{R}}] = \rho \sum_{i=0}^{N+1} \int_{\Omega_i} \text{Re}[\varphi_3] n_k ds, \quad (27)$$

$$b_{k3} = -\text{Re}[f_{k3}^{\text{R}}] = \rho\omega \sum_{i=0}^{N+1} \int_{\Omega_i} \text{Im}[\varphi_3] n_k ds. \quad (28)$$

2.6. Energy conversion efficiency, reflection coefficient, and transmission coefficient

The motion response ξ_3 of a PTO-integrated breakwater could be solved from the equation of motion in the frequency domain

$$[-\omega^2(m_{33} + a_{33}) - i\omega(b_{33} + b_{33}^{\text{PTO}}) + c_{33}]\xi_3 = F_3^{\text{EX}}, \quad (29)$$

where $m_{33} = \rho V$, a_{33} , b_{33} , b_{33}^{PTO} , and $c_{33} = \rho g S$ are the mass, added mass, radiation damping, PTO damping, and hydrostatic restoring stiffness of the float, respectively. F_3^{EX} is the wave excitation forces in heave. V is the displacement, and S is the area of the waterplane.

The time-averaged absorbed power is

$$P^{\text{ave}} = \frac{1}{2} \omega^2 b^{\text{PTO}} |\xi_3|^2. \quad (30)$$

The power in the incident per unit width of the wave front is [28]

$$P^{\text{wave}} = \frac{1}{4} \rho g A^2 \left(1 + \frac{2k_0 h}{\sinh 2k_0 h} \right) \frac{\omega}{k_0}. \quad (31)$$

The energy conversion efficiency of the PTO-integrated breakwater is

$$\eta = \frac{P^{\text{ave}}}{P^{\text{wave}}}. \quad (32)$$

The theoretical optimization of the PTO damping and the absorbed power could be obtained while the float is resonant in heave [29]. The results are briefly given as follows without detailed derivation,

$$b^{\text{opt}} = \frac{1}{\omega} \sqrt{[(m_{33} + a_{33})\omega^2 - c_{33}]^2 + \omega^2 b_{33}^2}, \quad (33)$$

where b^{opt} is the optimal PTO damping. The optimal absorbed power could be easily computed from Eq. (30).

While the velocity potential is solved, substitute Eqs.(10)-(13) into the equation of the reflection coefficient K_R and the transmission coefficient K_T , the expressions after simplification are

$$K_R = \left| \frac{\varphi^D - i\omega \xi_3 \varphi_3}{\varphi^I} \right|_{z=0, x=-\infty} = \left| R_{00}^{\Omega_0} + \frac{\omega^2 R_{03}^{\Omega_0} \xi_3}{gA} \right|, \quad (34)$$

$$K_T = \left| \frac{\varphi^I + \varphi^D - i\omega \xi_3 \varphi_3}{\varphi^I} \right|_{z=0, x=+\infty} = \left| R_{00}^{\Omega_{N+1}} + \frac{\omega^2 R_{03}^{\Omega_{N+1}} \xi_3}{gA} \right|. \quad (35)$$

3. Convergence study and verification

In this section, numerical computations are performed to conduct convergence study and validate the proposed semi-analytical method. On the basis of Section 2, the discretization number of breakwater N and the number of truncated eigen-function terms M and L in Eqs.(11)-(13) have a great influence on calculation results, so it is necessary to conduct convergence studies on these parameters. According to Eq. (32), the energy conversion efficiency is equal to P^{ave} over P^{wave} . For the preset wave, P^{wave} is fixed. And as Eq. (30) showed, P^{ave} is in connection with b^{PTO} and ξ_3 . When the optimization of the PTO damping is chosen, b^{opt} and ξ_3 are related to added mass, radiation damping and wave excitation force according to Eq. (29) and (33). So added mass, radiation damping and wave excitation force are chosen in convergence study. To validate the present semi-analytical method, a two-dimensional float with left triangular bottom [14], named T-left shown in the Table 1, which has been proved to have good wave energy conversion and coastal protection performance, is simulated in this section as an example. And the dimension parameters are shown in the Table 1. The heights of the vertical part and the triangular part are $l_1^B = 5.4$ m and $l_2^B = 1.8$ m, respectively, and the width is $w^B = 1.8$ m.

The present semi-analytical model is validated through three steps. The first step is a convergence test on the bottom shape asymptote. Aiming to eliminate the influence of truncation accuracy with large M and L , set $M = L = 200$. The added mass, radiation damping, and wave excitation force for different numbers of subdomains, $N = 8, 15$, and 30 , are in Figure 2a, b, and c. Results of hydrodynamic coefficients for $N = 15$ and $N = 30$ show good agreement with a maximum error of 1.03% for added mass, 0.63% for radiation damping, and

0.57% for wave excitation force, whereas the added mass for $N = 8$ shows a small deviation with a maximum error of 2.02%. Therefore, $N = 15$ is accurate enough for the float with left triangular bottom.

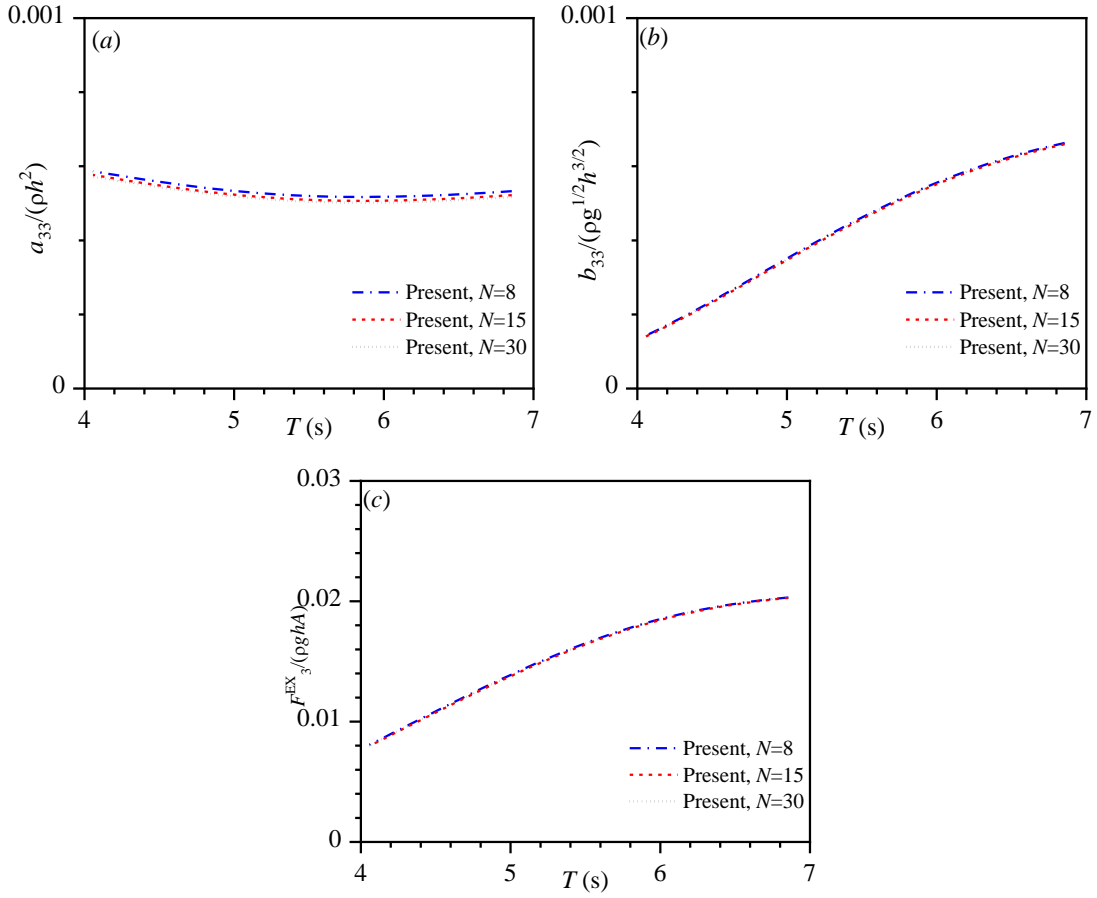
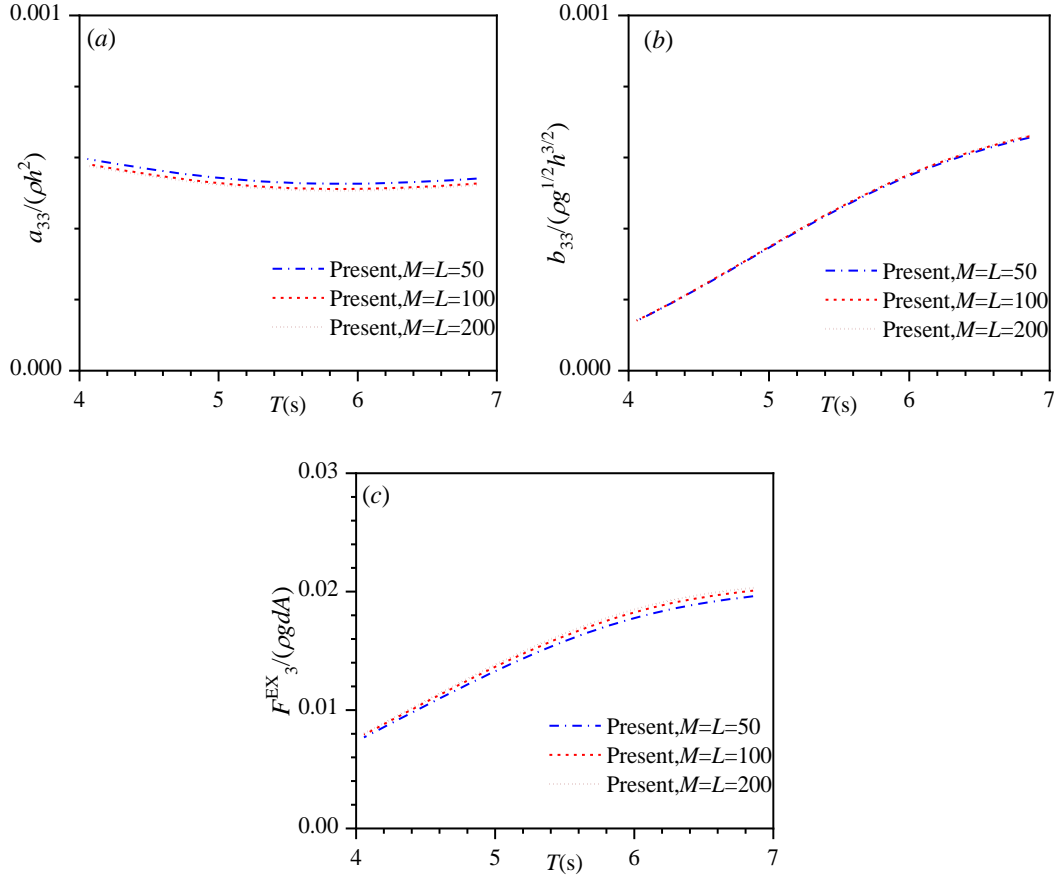


Figure 2 A convergence test on the bottom asymptote: comparative results in (a) added mass, (b) radiation damping, (c) wave excitation force

The second step is a convergence test on the truncation accuracy. The same model as in the convergence test is used. And the number of subdomains is set as $N = 15$. The added mass, radiation damping, and wave excitation force for different numbers of truncated terms, $M = L = 50, 100$, and 200 , are in Figure 3. Results of hydrodynamic coefficients for $M = L = 100$ and 200 are almost identical with a maximum error of 0.94% for added mass, 0.25% for radiation damping, and 1.40% for wave excitation force, whereas the added mass and the wave excitation force for $M = L = 50$ shows a small but obvious deviation, which is 2.89% and 2.83% respectively. Therefore, $M = L = 100$ is accurate enough for the float with left triangular bottom.

1



2

3

4

5

6

7

Figure 3 Convergence test on the truncation accuracy: comparative results in (a) added mass, (b) radiation damping, and (c) wave excitation force

The third step is an energy conservation test, as shown in Figure 4. The transmitted, reflected, and absorbed wave energy is conservative. So the reflection coefficient, transmission coefficient and efficiency are accurate.

8

9

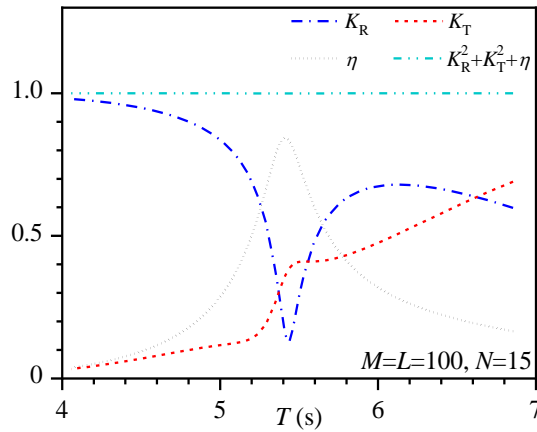


Figure 4 Energy conservation relationship

10

11

4. Effects of PTO damping and geometric asymmetry on the performance of a PTO-integrated breakwater

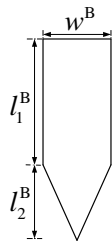
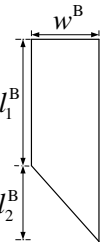
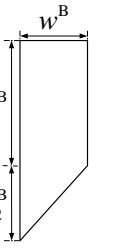
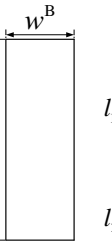
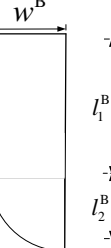

12

13

In this section, the effects of PTO damping and geometric asymmetry on the performance of a PTO-integrated breakwater are examined. The water depth is $h = 60$ m. The period T of the

incident wave is from 4 s to 7 s. The previous study showed the asymmetric float with triangular or hemisphere bottom has good wave energy conversion and wave attenuation performance [24][30]. However, the reasons were not given well. To study the effect of asymmetry and the bottom shape on the performance of a PTO-integrated breakwater, six models are used. The names of the models and their key dimensions of the immersed parts are shown in Table 1. “Tri” represents a symmetric triangular bottom, “T-” an asymmetric triangular bottom, “Rec” a flat bottom, “C-” a circular arc bottom, and “RC-” a reversed circular arc bottom. Similar with Section 3, the convergence study is carried out for all the other five models, $M=L=150, 100, 70$, 100, 150 for Tri, T-right, Rec, C-left and RC-left respectively, and $N=20, 8, 1, 10, 20$ are used in the following calculations.

Table 1 Configurations of symmetric and asymmetric PTO-integrated breakwaters

Models	Tri	T-left	T-right	Rec	C-left	RC-left
Cross-section						

4.1. Effect of PTO damping on wave attenuation

In this section, the influence of the PTO damping b^{PTO} on the transmission coefficient K_T is studied to examine if the implantation of a PTO system could improve the wave attenuation of a breakwater. The models ‘Tri’, ‘T-left’, and ‘T-right’ in Table 1 are used. Their drafts are equal. A series of linear PTO damping, $b^{\text{PTO}} = 0, 10^2, 10^4, 10^6 \text{ N}\cdot\text{s}/\text{m}$ and b^{opt} , are applied in each case. b^{opt} is the optimal value of PTO damping at the heaving natural period in each case, obtained by Eq. (33). The key parameters of the models are in Table 2. The results of the transmission coefficient K_T for different PTO damping b^{PTO} are displayed in Figure 5.

Table 2 Key parameters of Tri, T-left, and T-right models

Models	l_1^B (m)	l_2^B (m)	w^B (m)	d_s (m)	d_A (m)	γ	Heaving natural period (s)	b^{opt} (N·s/m)
Tri	6	0.6	1.8	6.6	0	0	5.38	304.14
T-left	6	0.6	1.8	6	0.6	−0.167	5.45	654.32
T-right	6	0.6	1.8	6	0.6	−0.167	5.45	1119.31

In the three PTO-integrated breakwaters, the trends of K_T for a given b^{PTO} are quite similar. Asymmetry does not affect the way the PTO damping influencing the wave attenuation of a PTO-integrated breakwater. While $b^{\text{PTO}} = 0$ and $10^2 \text{ N}\cdot\text{s}/\text{m}$, K_T obtains a trough between $T = 5 \text{ s}$ and 5.2 s . K_T is about 0 at the trough and is below 0.1 at smaller incident wave periods. K_T also obtains a peak of about 1.0 at the heaving natural period. While the PTO system is not installed on the breakwater or the PTO damping is small, the wave attenuation of the breakwater is excellent in a range of shorter waves (approximate $T \leq 5.2 \text{ s}$ in the selected cases). Waves of a particular period could be nearly all blocked. But the situation

worsens quickly as the waves become even a little longer. While the incident wave period matches the heaving natural period of the breakwater, the breakwater attenuates little wave energy. The wave attenuation without a PTO system or with a small PTO damping is inferior in longer waves. When $b^{\text{PTO}} = b^{\text{opt}}$, the local peak still occurs but is much smaller than those of $b^{\text{PTO}} = 0$ and $10^2 \text{ N}\cdot\text{s}/\text{m}$ and the trough vanishes. As b^{PTO} increases to 10^4 and $10^6 \text{ N}\cdot\text{s}/\text{m}$, the pattern of K_T further smooths and flattens. The local trough and peak both vanish and K_T monotonically increases as wave period T increases. While larger PTO damping is applied, wave attenuation is a little worse in shorter waves but the transmission coefficient K_T is still below 0.3, whereas the wave attenuation in longer waves is much better. The wave attenuation finally converges as the PTO damping continues to increase.

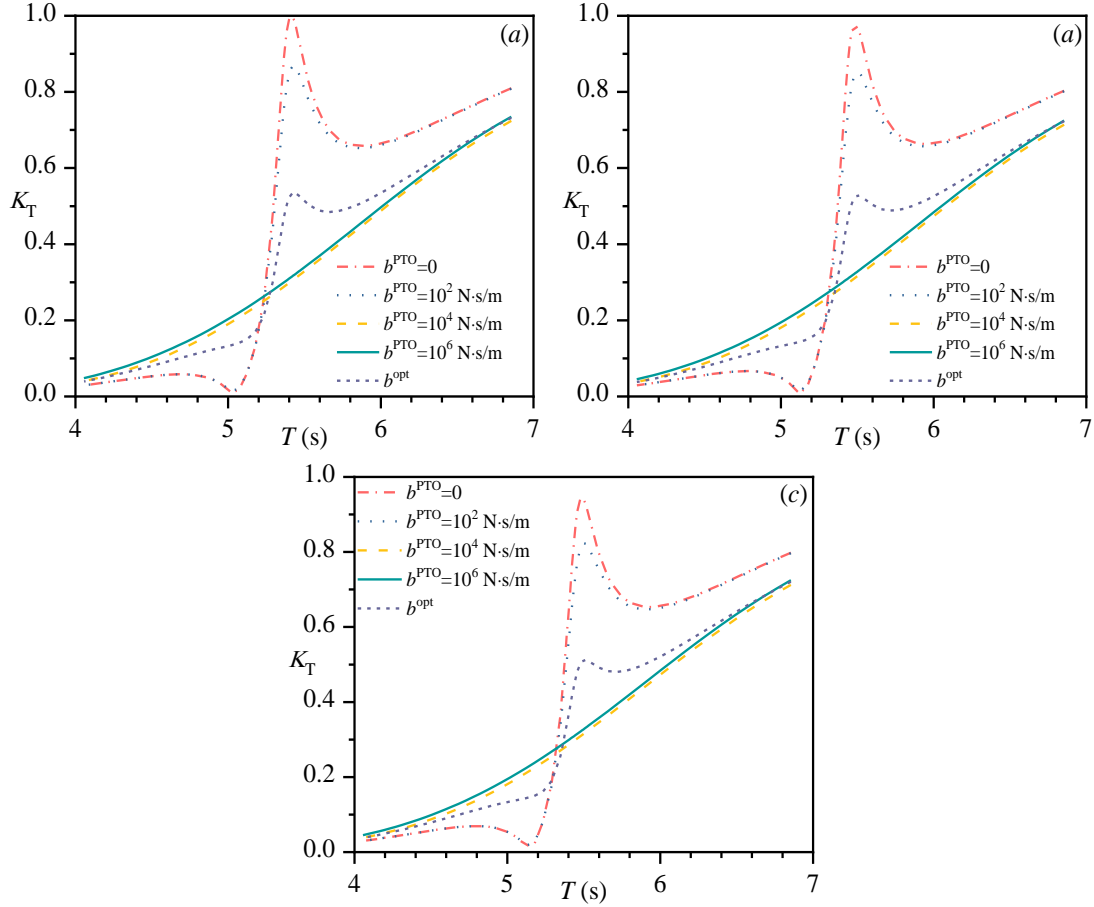


Figure 5 Effect of the PTO damping b^{PTO} on the transmission coefficient K_T for (a) Tri, (b) T-left, and (c) T-right. $l_1^B = 0.6 \text{ m}$, $l_2^B = 6 \text{ m}$, and $w^B = 1.8 \text{ m}$. $b^{\text{PTO}} = 0, 10^2, 10^4, 10^6 \text{ N}\cdot\text{s}/\text{m}$ and b^{opt} .

Practically, integrating a PTO system into a floating breakwater to build a hybrid system could not only help foster the extensive and commercial wave energy extraction but also improve the wave attenuation of the breakwater in longer waves, particularly suppressing wave transmission in the region around the heaving natural period.

4.2. Effect of asymmetry on energy conversion efficiency and wave attenuation

The influence of the DoA γ of a PTO-integrated breakwater on its transmission coefficient K_T , reflection coefficient K_R , and energy conversion efficiency η is studied in this part. The models ‘Tri’, ‘T-left’, and ‘T-right’ in Table 1 are used. The dimensions of Tri, T-left, and T-right, wave conditions, and water depth are the same as those in Section 4.1, so do their DoA

and absolute asymmetry. Here the PTO damping b^{PTO} achieves the optimal value b^{opt} in each case. Results are displayed in Figure 6.

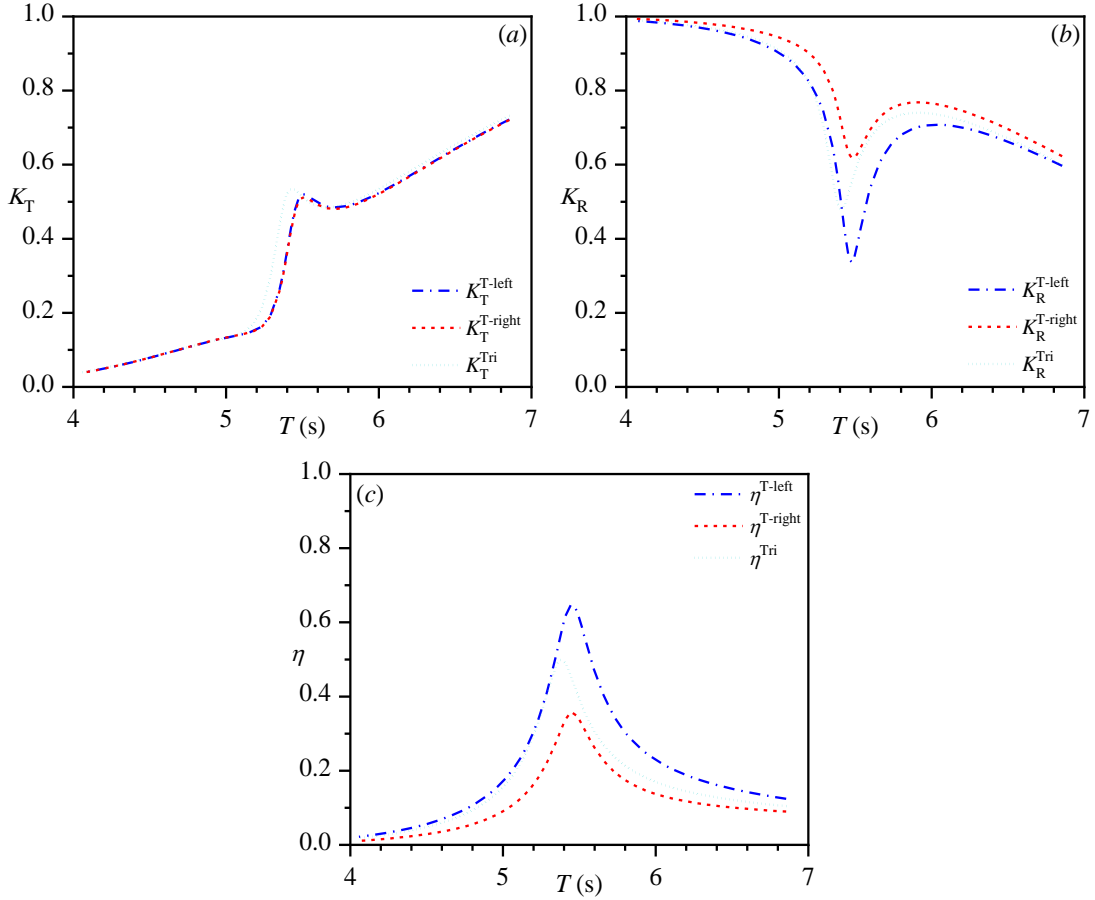


Figure 6 Effect of geometric asymmetry on (a) transmission coefficient K_T , (b) reflection coefficient K_R , and (c) energy conversion efficiency η of the “Tri”, “T-left”, and “T-right” PTO-integrated breakwaters. $l_1^B = 0.6$ m, $l_2^B = 6$ m, and $w^B = 1.8$ m. The PTO damping in each case takes its optimal value b^{opt} .

In Figure 6a, note that $K_T^{\text{T-left}}$ and $K_T^{\text{T-right}}$ are almost identical and K_T^{Tri} deviates a little from the other two. For a PTO-integrated breakwater with a fixed contour, although the sign of the DoA γ reverses due to the exchange of orientation of the walls, it does not affect the absolute asymmetry $|\gamma|$. And while the absolute asymmetry is fixed, the wave attenuation is fixed no matter its orientation. Further, if no PTO system is integrated, according to the conservation relationship $K_T^2 + K_R^2 = 1$, the reflection coefficient K_R is also not affected if the absolute asymmetry is not changed. Note that in the given incident period range, $K_T^{\text{T-left}} = K_T^{\text{T-right}} < K_T^{\text{Tri}}$ and $|\gamma^{\text{T-left}}| = |\gamma^{\text{T-right}}| > |\gamma^{\text{Tri}}|$. It is observed that larger absolute asymmetry yields slightly better wave attenuation. From the above analysis, the wave attenuation of a PTO integrated breakwater relies on the overall geometry and the absolute asymmetry, i.e., no matter the short wall or the long wall of the float facing the incident wave, the transmission coefficient remains unchanged.

In Figure 6b and Figure 6c, a local trough of K_R and a local peak of η occur at the heaving natural period of the PTO-integrated breakwater. While the PTO-integrated breakwater is in

resonance, it works well in absorbing the part of wave energy that is not transmitted. Roughly, the relationships of reflection coefficients and the efficiency are that $K_R^{T-left} < K_R^{Tri} < K_R^{T-right}$ and $\eta^{T-left} > \eta^{Tri} > \eta^{T-right}$. T-left has the best and T-right has the worst energy conversion efficiency among the three. As also $\gamma^{T-right} > \gamma^{Tri} > \gamma^{T-left}$, the energy conversion efficiency of a PTO-integrated breakwater depends on its DoA. The comparative results show that the DoA does not change the total amount of the reflected and absorbed wave energy but influences their proportions. As the DoA increases, i.e., the leeward accumulation of displacement being faster, the proportion of absorbed energy increases, hence the energy conversion efficiency is improved.

In application, approaches intending to improve the wave attenuation ability of a PTO-integrated breakwater by merely modifying the contour of the seaward wall without changing the absolute asymmetry may have very limited effort. The structure should be highly asymmetric and the displacement should concentrate on the lee side.

5. Approaches to change the geometric asymmetry of a triangular-wedge PTO-integrated breakwater

In the previous section, the roles of DoA and absolute asymmetry in the energy conversion efficiency and wave attenuation of a PTO-integrated breakwater have been investigated. It was found that enlarging the absolute asymmetry could improve the wave attenuation and enlarging the DoA could improve the energy conversion efficiency. Here are three approaches to change the absolute asymmetry or the DoA of a PTO-integrated breakwater with a triangular-wedge bottom by modifying: 1) the bottom slope, 2) the contour of the wedge, and 3) the width. Parametric studies are carried out to 1) demonstrate the feasibility and applicability of the findings in the previous section, and 2) examine the effect of the three approaches in influencing the performance of the PTO-integrated breakwater.

5.1. Bottom slope

The influence of the bottom slope on the energy conversion efficiency and wave attenuation of a triangular-wedge PTO-integrated breakwater is investigated. The models ‘T-left’, ‘T-right’, and ‘Rec’ in Table 1 are used. Keep the drafts of the models equal. The PTO damping b^{PTO} in each case achieves its optimal value b^{opt} . The key parameters of the selected models are in Table 3. Note that for T-left, the DoA increases as the bottom slope of the structure increases; for T-right, the DoA decreases as the bottom slope increases. Since $K_T^{T-left} = K_T^{T-right}$ for a fixed absolute asymmetry, the results of transmission coefficients of T-left and T-right are collectively given in Figure 7. The reflection coefficient K_R and the energy conversion efficiency η of T-left are in Figure 8. Those of T-right are in Figure 9.

Table 3 Key parameters of T-left models with different bottom slope

Models	l_1^B (m)	l_2^B (m)	w^B (m)	d_s (m)	d_A (m)	γ	Heaving natural period (s)
T-left/T-right	6.6	0.6	1.8	6.6	0.6	+/-0.167	5.68

T-left/T-right	6.0	1.2	1.8	6.0	1.2	$+/-0.333$	5.55
T-left/T-right	5.4	1.8	1.8	5.4	1.8	$+/-0.5$	5.41
Rec	$l^B = 7.2$ m		1.8	6.3	0	0	5.80

In Figure 7, Figure 8, and Figure 9, the peaks of K_T , K_R , and η respectively deviate for different models due to their different natural periods, but one can still find the following facts. As shown in Figure 7, K_T decreases as l_2^B increases, but the change is not very large, particularly in the regions away from the heaving natural period. The wave attenuation of a PTO-integrated breakwater at the natural period is slightly improved as its bottom slope and absolute asymmetry are increased.

In Figure 8 and Figure 9, K_R^{T-left} decreases and η^{T-left} increases as l_2^B increases. $K_R^{T-right}$ increases and $\eta^{T-right}$ decreases as l_2^B increases. The energy conversion efficiency of T-left and T-right show opposite trends as the bottom slope changes. While the DoA is referred to, the opposite trends reveal the same fact: as the DoA of a PTO-integrated breakwater is enlarged, its energy conversion efficiency is improved, particularly in the narrow region around the heaving natural period. This result is consistent with the findings in the previous section.

To increase the energy conversion efficiency and wave attenuation of a triangular-wedge PTO-integrated breakwater, one needs to make the shorter wall face the incident wave and increase the bottom slope.

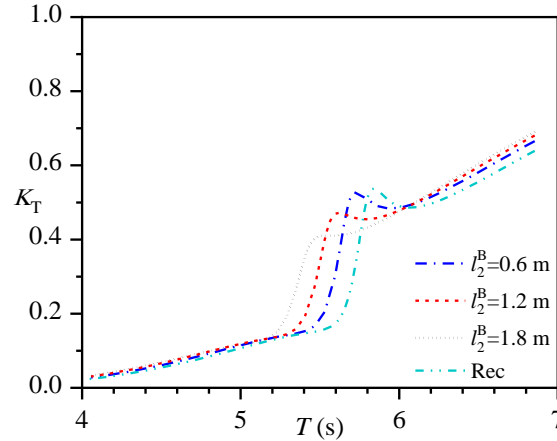


Figure 7 Influence of bottom slope on the transmission coefficient K_T of the “T-left”, “T-right” and “Rec” PTO-integrated breakwaters. $l^B = 7.2$ m, $l_1^B = 6.6, 6$, and 5.4 m, the corresponding $l_2^B = 0.6, 1.2$, and 1.8 m, $w^B = 1.8$ m. The PTO damping in each case takes its optimal value b^{opt} .

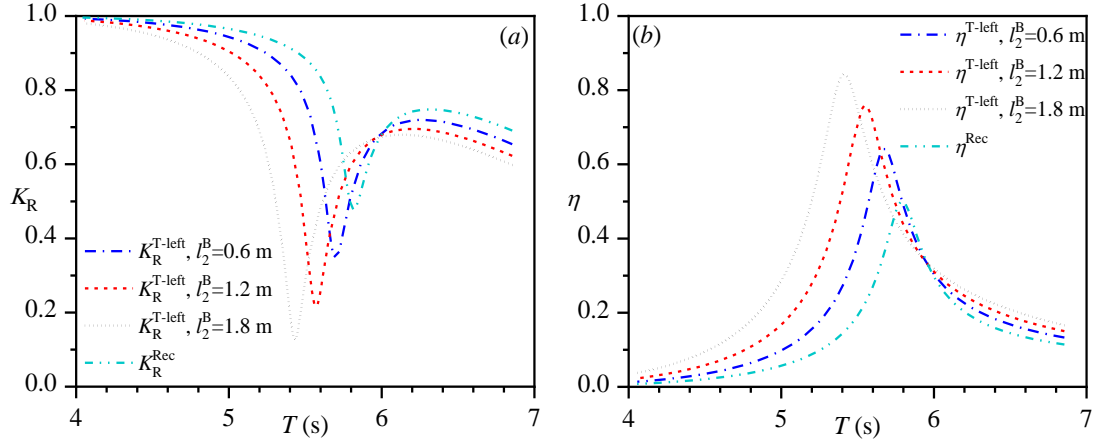


Figure 8 Effect of bottom slope on the (a) reflection coefficient K_R and (b) energy conversion efficiency η of the “T-left” and “Rec” PTO-integrated breakwaters. $l^B = 7.2$ m, $l_1^B = 6.6, 6$, and 5.4 m, the corresponding $l_2^B = 0.6, 1.2$, and 1.8 m, $w^B = 1.8$ m. The PTO damping in each case takes its optimal value b^{opt} .

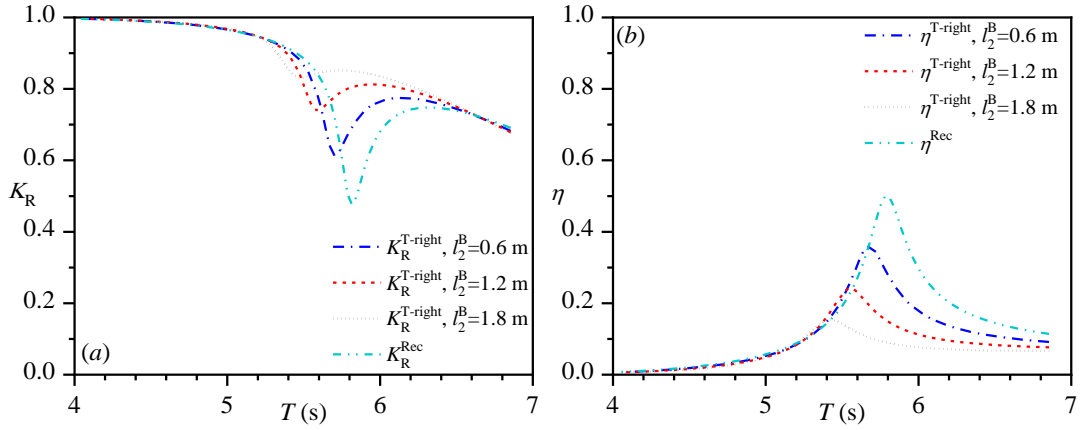


Figure 9 Effect of bottom slope on the (a) reflection coefficient K_R and (b) energy conversion efficiency η of the “T-right” and “Rec” PTO-integrated breakwaters. $l^B = 7.2$ m, $l_1^B = 6.6, 6$, and 5.4 m, the corresponding $l_2^B = 0.6, 1.2$, and 1.8 m, $w^B = 1.8$ m. The PTO damping in each case takes its optimal value b^{opt} .

5.2. Contour of wedge

The influence of the bottom wedge contour of a “left” type PTO-integrated breakwater on its energy conversion efficiency and wave attenuation is studied. The models ‘T-left’, ‘C-left’, and ‘RC-left’ in Table 1 are selected. The drafts of the models are equal. The PTO damping b^{PTO} in each case achieves its optimal value b^{opt} . The key parameters are given in Table 4. Results of the transmission coefficient K_T , the reflection coefficient K_R , and the energy conversion efficiency η of T-left, C-left, and RC-left are in Figure 10.

Table 4 Key parameters of T-left, C-left, and RC-left models

Models	l_1^B (m)	l_2^B (m)	w^B (m)	d_S (m)	d_A (m)	γ	Heaving natural period (s)
T-left	5.4	1.8	1.8	5.4	1.8	0.5	5.41

C-left	5.4	1.8	1.8	5.4	1.8	0.218	5.57
RC-left	5.4	1.8	1.8	5.4	1.8	0.798	5.35

In Figure 10a, $K_T^{\text{RC-left}} < K_T^{\text{T-left}} < K_T^{\text{C-left}}$ in the region near the natural period. For the three cases, there is the relationship of DoA $\gamma^{\text{C-left}} < \gamma^{\text{T-left}} < \gamma^{\text{RC-left}}$. Then K_T decreases as γ increases. In Figure 10b and Figure 10c, it is observed that $K_R^{\text{T-left}} < K_R^{\text{C-left}}$ and $\eta^{\text{T-left}} > \eta^{\text{C-left}}$. $K_R^{\text{RC-left}}$ and $\eta^{\text{RC-left}}$ deviate horizontally a little from their counterparts due to a different heaving natural period. However, one can still approximately consider that $K_R^{\text{RC-left}} < K_R^{\text{T-left}} < K_R^{\text{C-left}}$ and $\eta^{\text{RC-left}} > \eta^{\text{T-left}} > \eta^{\text{C-left}}$ according to the pattern. As the DoA is increased by applying a reversed circular arc bottom contour, the energy conversion efficiency and wave attenuation are improved.

In practice, while using the RC-left design or similar scenario, one can improve the energy conversion efficiency and wave attenuation while simultaneously reducing the displacement, therefore save the cost of construction material.

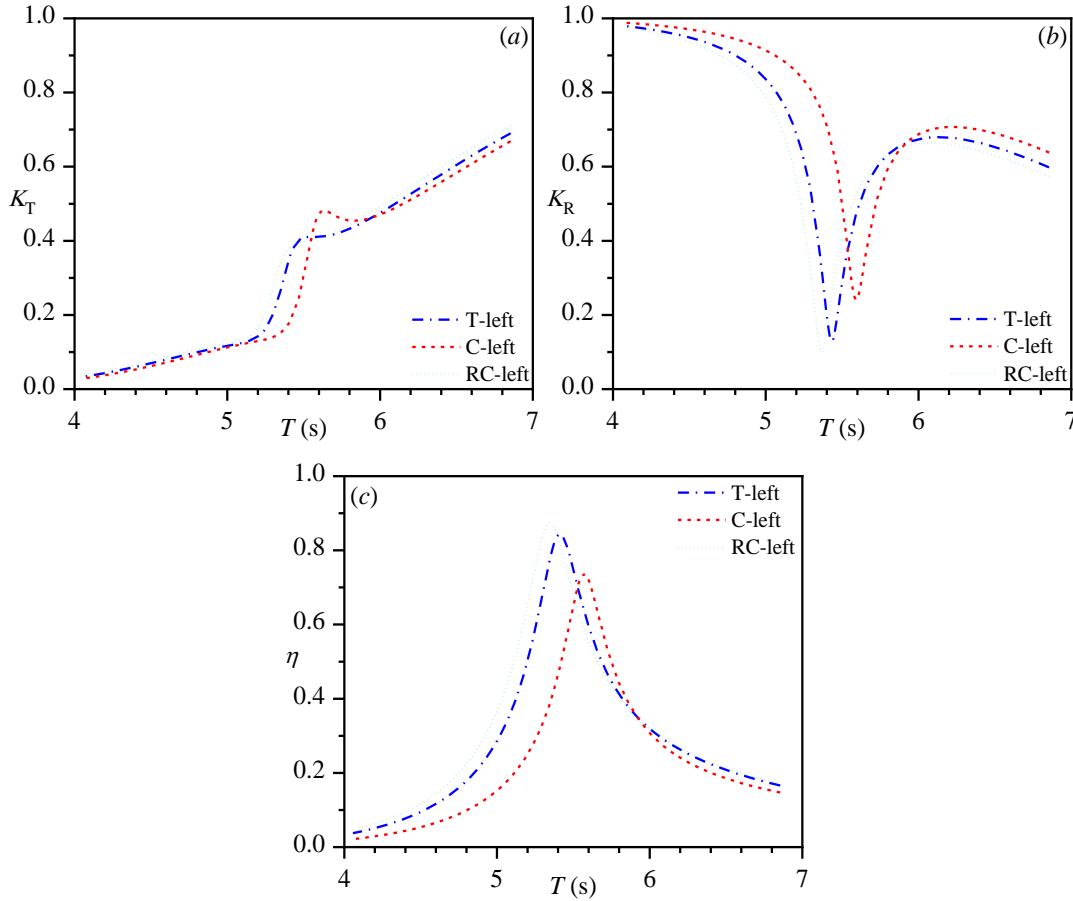


Figure 10 Effect of the contour of the wedge on the (a) transmission coefficient K_T , (b) reflection coefficient K_R , and (c) energy conversion efficiency η of the “T-left”, “C-left”, and “RC-left” PTO-integrated breakwaters. $l_1^B = 5.4$ m, the corresponding $l_2^B = 1.8$ m, $w^B = 1.8$ m. The PTO damping in each case takes its optimal value b^{opt} .

5.3. Width

In this section, the influence of the width w^B of a T-left PTO-integrated breakwater on its energy conversion efficiency and wave attenuation is studied. Here the drafts of the models are equal. The PTO damping b^{PTO} in each case achieves its optimal value b^{opt} . The key

parameters are given in Table 5. Note that as w^B increases, the DoA γ decreases. Results of the transmission coefficient K_T , the reflection coefficient K_R , and the energy conversion efficiency η are shown in Figure 11.

Table 5 Key parameters of T-left models with different width

Models	l_1^B (m)	l_2^B (m)	w^B (m)	d_S (m)	d_A (m)	γ	Heaving natural period (s)
T-left	5.4	1.8	1.2	5.4	1.8	0.188	5.52
T-left	5.4	1.8	1.8	5.4	1.8	0.125	5.41
T-left	5.4	1.8	2.4	5.4	1.8	0.094	5.30

In Figure 11a, the trends of K_T of the three PTO-integrated breakwaters are the same. The horizontal deviation is due to the different heaving natural periods. As w^B increases, K_T is smaller in shorter waves and longer waves but is more prominent in the narrow region around the heaving natural period. Enlarging the width of a breakwater could improve its wave attenuation regardless that the structure is symmetric or asymmetric, which is also observed in previous investigations [14][30]. But the simultaneous decrease of DoA caused by the increase in width will weaken the wave attenuation. In the regions of shorter and longer waves away from the heaving natural period, the variation of width has a more decisive influence than the DoA. The improvement in wave attenuation due to the increase of width surpasses the wave attenuation reduction due to the loss of the DoA. Whereas in the region near the heaving natural period, wave attenuation is dominated by the DoA rather than the variation of width. The consequences are therefore reversed.

In Figure 11b and Figure 11c, the variation of w^B does not change K_R and η a lot but deviates the heaving natural period. As w^B increases, K_R increases and η decreases. Like the regularities in wave attenuation, the energy conversion efficiency is weakened in the region around the heaving natural period but is slightly improved in the regions of shorter and longer waves. Besides, increasing the width could move the energy conversion efficiency peak toward longer waves.

Considering a flat-bottom PTO-integrated breakwater, enlarging its width will cause no loss in the DoA. Its wave attenuation could be improved in the entire frequency domain and the energy conversion peak will be slightly enhanced and moved toward longer waves, as revealed in Refs [14]. For instance, however, while enlarging the width of a triangular-wedge PTO-integrated breakwater, the loss of DoA also happens and causes a reduction in the energy conversion efficiency and wave attenuation, particularly in the region near the heaving natural period. Based on the above analysis, while using the variation of the width to change the DoA of a triangular-wedge PTO integrated breakwater, one needs to consider the trade-off between the two contradicting effects carefully. Besides, the change of cost due to the variation of width should also be considered.

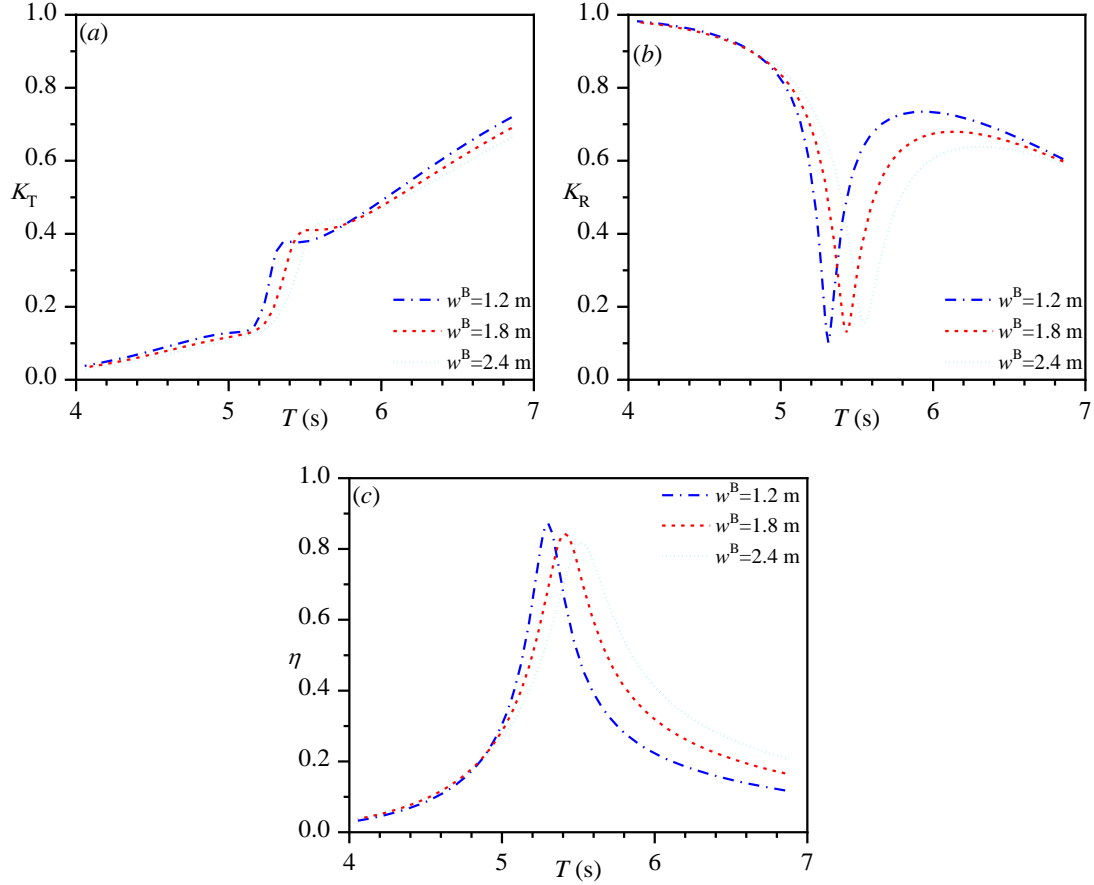


Figure 11 Effect of the width on the (a) transmission coefficient K_T , (b) reflection coefficient K_R , and (c) energy conversion efficiency η of "T-left" breakwater. $l_1^B = 5.4$ m, $l_2^B = 1.8$ m. $w^B = 1.2, 1.8$, and 2.4 m. The PTO damping in each case takes its optimal value b^{opt} .

6. Conclusions

The role of geometric asymmetry in the energy conversion efficiency and wave attenuation of a PTO-integrated breakwater was investigated. A 2D frequency-domain semi-analytical model dealing with floats with arbitrary bottom shapes is established based on the linear potential flow theory. The method of matching eigenfunction is applied to solve the diffracted and radiated potential. The model is validated against through convergent tests and the law of conservation of energy. The concepts of the degree of asymmetry and the absolute asymmetry are introduced and their mathematical expressions are given to quantify and compare the geometric asymmetry of different PTO-integrated breakwaters. The effects of PTO damping, degree of asymmetry, and absolute asymmetry on the transmission coefficient, reflection coefficient, and energy conversion efficiency are observed and analyzed. Significant remarks are concluded as follows:

1) While viscosity is not considered, a bare floating breakwater is nearly useless in attenuating wave energy at its heaving natural period. Applying a PTO-integrated breakwater could improve the wave attenuation in longer waves, particularly near the heaving natural period of the system.

2) For a PTO-integrated breakwater with a fixed absolute asymmetry, no matter which wall faces the incident waves, the wave attenuation is not influenced. The variation of the degree of

asymmetry of an asymmetric PTO-integrated breakwater caused by the exchange of orientation of the two walls does not change the total amount of the reflected and absorbed wave energy but influences their proportions. An increase in the degree of asymmetry improves the energy conversion efficiency and wave attenuation, particularly in the region near the heaving natural period. In order to capture more wave power, the shorter wall of the PTO-integrated breakwater should face the incident wave.

3) Based on the findings in the influence of geometric asymmetry, three approaches to modify the energy conversion efficiency and wave attenuation properties of a triangular-bottom PTO-integrated breakwater, including changing the bottom slope, the contour of the wedge, and the width, are examined. Increasing the bottom slope could effectively improve energy conversion efficiency and wave attenuation. Using a reversed circular arc bottom or similar configuration could improve the energy conversion efficiency and wave attenuation. By increasing the width, the energy conversion efficiency and wave attenuation decline in the region near the heaving natural period but are slightly improved in the regions of shorter and longer waves. The peak of energy efficiency could also be moved slightly toward the longer waves. In practical application, one should carefully consider the advantages and disadvantages of the approaches and the consequent manufacturing cost.

Acknowledgments

This work was supported by the National Natural Science Foundation of China (52071096). S.Z. gratefully acknowledges the State Key Laboratory of Ocean Engineering, Shanghai Jiao Tong University, China for supporting part of this work through the Open Research Fund Program (Grant No. 1916).

Appendix

The expression of the coefficient matrices \mathbf{A} in Eq. (23) is

$$\mathbf{A} = \begin{pmatrix} \mathbf{A}_{M+1,M+1}^{\Omega_0,v} & \mathbf{A}_{M+1,2L+2}^{\Omega_1,v} \\ \mathbf{A}_{L+1,M+1}^{\Omega_0,p} & \mathbf{A}_{L+1,2L+2}^{\Omega_1,p} \\ & \mathbf{A}_{L+1,2L+2}^{\Omega_i,v} & \mathbf{A}_{L+1,2L+2}^{\Omega_{i+1},v} \\ & \mathbf{A}_{L+1,2L+2}^{\Omega_i,p} & \mathbf{A}_{L+1,2L+2}^{\Omega_{i+1},p} \\ & & \mathbf{A}_{L+1,2L+2}^{\Omega_N,p} & \mathbf{A}_{L+1,M+1}^{\Omega_{N+1},p} \\ & & \mathbf{A}_{M+1,2L+2}^{\Omega_N,v} & \mathbf{A}_{M+1,M+1}^{\Omega_{N+1},v} \end{pmatrix}. \quad (36)$$

In the superscripts, Ω_i means that this part of coefficients are associated with the unknowns in the expression of velocity potential in the subdomain Ω_i , “ v ” means that the coefficients are for the unknowns to satisfy the conditions of continuous normal velocity, and “ p ” for continuous pressure. Giving the following definition

$$\begin{cases} Q_0 = \int_{-h}^0 Z_0^2(k_0 z) dz = \frac{1}{\cosh^2(k_0 h)} \left(\frac{h}{2} + \frac{\sinh(2k_0 h)}{4k_0} \right), \\ Q_m = \int_{-h}^0 Z_m^2(k_m z) dz = \frac{1}{\cos^2(k_m h)} \left(\frac{h}{2} + \frac{\sin(2k_m h)}{4k_m} \right), \end{cases} \quad m = 1, \dots, M, \quad (37)$$

the data range of the number of truncated eigen-function terms are that $m = 1, \dots, M$ and $l = 1, \dots, L$,

$$\begin{cases}
A_{0,0}^{\Omega_0,v} = -ik_0 Q_0, \\
A_{m,m}^{\Omega_0,v} = k_m Q_m, \\
A_{m,l}^{\Omega_1,v} = e^{\lambda_l^{\Omega_1} x_0} \lambda_l^{\Omega_1} \int_{-h}^{-d_1} Y_l(\lambda_l^{\Omega_1} z) Z_m(k_m z) dz, \\
A_{m,L+1}^{\Omega_1,v} = \int_{-h}^{-d_1} Y_0(\lambda_0^{\Omega_1} z) Z_m(k_m z) dz, \\
A_{m,L+l}^{\Omega_1,v} = -e^{-\lambda_l^{\Omega_1} x_0} \lambda_l^{\Omega_1} \int_{-h}^{-d_1} Y_l(\lambda_l^{\Omega_1} z) Z_m(k_m z) dz, \\
A_{l,m}^{\Omega_0,p} = \frac{2}{h-d_1} \int_{-h}^{-d_1} Z_m(k_m z) Y_l(\lambda_l^{\Omega_1} z) dz, \\
A_{0,0}^{\Omega_1,p} = 1, \\
A_{l,l}^{\Omega_1,p} = e^{\lambda_l^{\Omega_1} x_0}, \\
A_{0,L+1}^{\Omega_1,p} = x_0, \\
A_{l,L+l}^{\Omega_1,p} = e^{-\lambda_l^{\Omega_1} x_0}.
\end{cases} \quad (38)$$

For $i = 1, \dots, N-1$, the expressions of the submatrix of the coefficient matrices \mathbf{A} are as follows:

$$\begin{cases}
A_{0,0}^{\Omega_i,p} = \frac{(h-d_i)}{2}, \\
A_{l,l}^{\Omega_i,p} = e^{\lambda_l^{\Omega_i} x_i} \frac{(h-d_i)}{2}, \\
A_{L+1,L+1}^{\Omega_i,p} = x_i \frac{(h-d_i)}{2}, \\
A_{L+l,L+l}^{\Omega_i,p} = e^{-\lambda_l^{\Omega_i} x_i} \frac{(h-d_i)}{2}, \\
A_{l,0}^{\Omega_i,p} = \int_{-h}^{-d_i} Y_0(\lambda_0^{\Omega_i} z) Y_l(\lambda_l^{\Omega_i} z) dz, \\
A_{l,l}^{\Omega_i,p} = e^{\lambda_l^{\Omega_i} x_i} \int_{-h}^{-d_i} Y_l(\lambda_l^{\Omega_i} z) Y_l(\lambda_l^{\Omega_i} z) dz, \\
A_{l,L+1}^{\Omega_i,p} = x_i \int_{-h}^{-d_i} Y_0(\lambda_0^{\Omega_i} z) Y_l(\lambda_l^{\Omega_i} z) dz, \\
A_{l,L+l}^{\Omega_i,p} = e^{-\lambda_l^{\Omega_i} x_i} \int_{-h}^{-d_i} Y_l(\lambda_l^{\Omega_i} z) Y_l(\lambda_l^{\Omega_i} z) dz, \\
A_{l,l}^{\Omega_i,v} = e^{\lambda_l^{\Omega_i} x_i} \lambda_l^{\Omega_i} \int_{-h}^{-d_i} Y_l(\lambda_l^{\Omega_i} z) Y_l(\lambda_l^{\Omega_i} z) dz, \\
A_{l,L+1}^{\Omega_i,v} = \int_{-h}^{-d_i} Y_l(\lambda_l^{\Omega_i} z) Y_0(\lambda_0^{\Omega_i} z) dz, \\
A_{l,L+l}^{\Omega_i,v} = -e^{-\lambda_l^{\Omega_i} x_i} \lambda_l^{\Omega_i} \int_{-h}^{-d_i} Y_l(\lambda_l^{\Omega_i} z) Y_l(\lambda_l^{\Omega_i} z) dz, \\
A_{l,l}^{\Omega_i,v} = \frac{e^{\lambda_l^{\Omega_i} x_i} \lambda_l^{\Omega_i} (h-d_i)}{2}, \\
A_{l,L+1}^{\Omega_i,v} = \frac{(h-d_i)}{2}, \\
A_{l,L+l}^{\Omega_i,v} = \frac{-e^{-\lambda_l^{\Omega_i} x_i} \lambda_l^{\Omega_i} (h-d_i)}{2},
\end{cases} \quad (39)$$

$$\begin{cases}
A_{0,0}^{\Omega_N,p} = 1, \\
A_{l,l}^{\Omega_N,p} = e^{\lambda_l^{\Omega_N} x_N}, \\
A_{l,L+1}^{\Omega_N,p} = x_N, \\
A_{l,L+l}^{\Omega_N,p} = e^{-\lambda_l^{\Omega_N} x_N}, \\
A_{l,m}^{\Omega_{N+1},p} = \frac{\int_{-h}^{-d_N} 2Z_m(k_m z) Y_l(\lambda_l^{\Omega_N} z) dz}{(h-d_N)}, \\
A_{m,l}^{\Omega_N,v} = e^{\lambda_l^{\Omega_N} \lambda_l^{\Omega_N} \int_{-h}^{-d_N} Y_l(\lambda_l^{\Omega_N} z) Z_m(k_m z) dz}, \\
A_{m,L+1}^{\Omega_N,v} = \int_{-h}^{-d_N} Y_0(\lambda_0^{\Omega_N} z) Z_m(k_m z) dz, \\
A_{m,L+l}^{\Omega_N,v} = -e^{-\lambda_l^{\Omega_N} \lambda_l^{\Omega_N} \int_{-h}^{-d_N} Y_l(\lambda_l^{\Omega_N} z) Z_m(k_m z) dz}, \\
A_{0,0}^{\Omega_{N+1},v} = ik_0 Q_0, \\
A_{m,m}^{\Omega_{N+1},v} = -k_m Q_m.
\end{cases} \quad (40)$$

with the rest components in the coefficient matrix in Eq. (36) being zeros.

The expression of \mathbf{B}_j in Eq. (23) is as follows:

$$\mathbf{B}_j = \begin{bmatrix} B_{0j}^{x_0,v}, \dots, B_{Mj}^{x_0,v}, B_{0j}^{x_0,p}, \dots, B_{Lj}^{x_0,p}, B_{0j}^{x_i,v}, \dots, B_{Lj}^{x_i,v}, B_{0j}^{x_i,p}, \dots, \\ B_{Lj}^{x_i,p}, B_{0j}^{x_{N+1},p}, \dots, B_{Lj}^{x_{N+1},p}, B_{0j}^{x_{N+1},v}, \dots, B_{Mj}^{x_{N+1},v} \end{bmatrix}^T. \quad (41)$$

In the superscript, x_i means that the coefficient is associated with the vertical boundary at x_i . In detail,

$$\begin{cases} B_{00}^{x_0,v} = -ik_0 Q_0 \\ B_{m0}^{x_0,v} = 0, \quad m = 1, \dots, M \end{cases} \quad (42)$$

For $m = 0, \dots, M$ and $l = 0, \dots, L$,

$$B_{m3}^{x_0,v} = \int_{-h}^{-d_1} \frac{i\omega x_0}{h-d_1} Z_m(k_m z) dz, \quad (43)$$

$$B_{l3}^{x_0,p} = -\frac{i\omega}{(h-d_1)^2} \int_{-h}^{-d_1} [(z+h)^2 - x_0^2] Y_n(\lambda_l^{\Omega_0} z) dz, \quad (44)$$

$$B_{l3}^{x_i,v} = \frac{i\omega x_i}{h-d_i} \int_{-h}^{-d_i} Y_l(\lambda_l^{\Omega_i} z) dz - \frac{i\omega x_i}{h-d_i} \int_{-h}^{-d_i} Y_l(\lambda_l^{\Omega_i} z) dz \quad (45)$$

$$B_{l3}^{x_i,p} = \int_{-h}^{-d_i} \left(\frac{i\omega}{2(h-d_i)} - \frac{i\omega}{2(h-d_i)} \right) [(z+h)^2 - x_i^2] Y_l(\lambda_l^{\Omega_i} z) dz, \quad (46)$$

$$B_{l3}^{x_{N+1},p} = -\frac{i\omega}{(h-d_N)^2} \int_{-h}^{-d_N} [(z+h)^2 - x_N^2] Y_l(\lambda_l^{\Omega_N} z) dz, \quad (47)$$

$$B_{m3}^{x_{N+1},v} = \int_{-h}^{-d_N} \frac{i\omega x_N}{h-d_N} Z_m(k_m z) dz, \quad (48)$$

References

- [1] Ning, D. Z., Wang, R. Q., Zou, Q. P., & Teng, B. (2016). An experimental investigation of hydrodynamics of a fixed OWC Wave Energy Converter. *Applied Energy*, 168, 636-648.
- [2] Perez-Collazo, C., Greaves, D., & Iglesias, G. (2018). Hydrodynamic response of the WEC sub-system of a novel hybrid wind-wave energy converter. *Energy Conversion and Management*, 171, 307-325.
- [3] Zhou, Y., Ning, D., Shi, W., Johanning, L., & Liang, D. (2020). Hydrodynamic investigation on an OWC wave energy converter integrated into an offshore wind turbine monopile. *Coastal Engineering*, 162, 103731.
- [4] Cheng, Y., Xi, C., Dai, S., Ji, C., Cocard, M., Yuan, Z., & Incecik, A. (2021). Performance

- characteristics and parametric analysis of a novel multi-purpose platform combining a moonpool-type floating breakwater and an array of wave energy converters. *Applied Energy*, 292, 116888.
- [5] Hu, J., Zhou, B., Vogel, C., Liu, P., Willden, R., Sun, K., ... & Collu, M. (2020). Optimal design and performance analysis of a hybrid system combining a floating wind platform and wave energy converters. *Applied Energy*, 269, 114998.
- [6] Falnes, J. (2007). A review of wave-energy extraction. *Marine structures*, 20(4), 185-201.
- [7] Dai, J., Wang, C. M., Utsunomiya, T., & Duan, W. (2018). Review of recent research and developments on floating breakwaters. *Ocean Engineering*, 158, 132-151.
- [8] Ning, D. Z., Zhou, Y., Mayon, R., & Johanning, L. (2020). Experimental investigation on the hydrodynamic performance of a cylindrical dual-chamber Oscillating Water Column device. *Applied Energy*, 260, 114252.
- [9] Zheng, S., Antonini, A., Zhang, Y., Greaves, D., Miles, J., & Iglesias, G. (2019). Wave power extraction from multiple oscillating water columns along a straight coast. *Journal of Fluid Mechanics*, 878, 445-480.
- [10] Xu, C., & Huang, Z. (2018). A dual-functional wave-power plant for wave-energy extraction and shore protection: A wave-flume study. *Applied Energy*, 229, 963-976.
- [11] Zhang, H., Zhou, B., Vogel, C., Willden, R., Zang, J., & Geng, J. (2020). Hydrodynamic performance of a dual-floater hybrid system combining a floating breakwater and an oscillating-buoy type wave energy converter. *Applied Energy*, 259, 114212.
- [12] Reabroy, R., Zheng, X., Zhang, L., Zang, J., Yuan, Z., Liu, M., ... & Tiaple, Y. (2019). Hydrodynamic response and power efficiency analysis of heaving wave energy converter integrated with breakwater. *Energy Conversion and Management*, 195, 1174-1186.
- [13] Zhang, H., Zhou, B., Zang, J., Vogel, C., Fan, T., & Chen, C. (2021). Effects of narrow gap wave resonance on a dual-floater WEC-breakwater hybrid system. *Ocean Engineering*, 225, 108762.
- [14] Zhang, H., Zhou, B., Vogel, C., Willden, R., Zang, J., & Zhang, L. (2020). Hydrodynamic performance of a floating breakwater as an oscillating-buoy type wave energy converter. *Applied Energy*, 257, 113996.
- [15] Ning, D., Zhao, X., Götteman, M., & Kang, H. (2016). Hydrodynamic performance of a pile-restrained WEC-type floating breakwater: An experimental study. *Renewable Energy*, 95, 531-541.
- [16] Ma, Z., Mao, Y., Cheng, Y., & Zhai, G. (2019). Effect of the PTO Damping Force on the 2D Oscillating Buoy Wave Energy Converter Integrated into a Pile-Restrained Floating Breakwater. *Iranian Journal of Science and Technology, Transactions of Mechanical Engineering*, 1-13.
- [17] Zhao, X. L., Ning, D. Z., Götteman, M., & Kang, H. G. (2017). Effect of the PTO damping force on the wave pressures on a 2-D wave energy converter. *Journal of Hydrodynamics, Ser. B*, 29(5), 863-870.
- [18] Chen, B., Bruce, T., Greated, C. A., & Kang, H. (2017). Dynamic behavior of a wave power buoy with interior on-board linear generator. *Ocean Engineering*, 129, 374-381.
- [19] Ning, D. Z., Zhao, X. L., Zhao, M., Hann, M., & Kang, H. G. (2017). Analytical investigation of hydrodynamic performance of a dual float WEC-type breakwater. *Applied Ocean Research*, 65, 102-111.

- 1 [20]Guo, B., Wang, R., Ning, D., Chen, L., & Sulisz, W. (2020). Hydrodynamic performance
2 of a novel WEC-breakwater integrated system consisting of triple dual-freedom floats.
3 Energy, 209, 118463.
- 4 [21]Zhang, H., Zhou, B., Zang, J., Vogel, C., Jin, P., Ning, D. (2021). Optimization of a three-
5 dimensional hybrid system combining a floating breakwater and a wave energy converter
6 array. Energy Conversion and Management, 247:114717.
- 7 [22]Mei, C. C. (1989). The Applied Dynamics of Ocean Surface Waves. World Scientific,
8 Singapore.
- 9 [23]Madhi, F., Sinclair, M. E., & Yeung, R. W. (2014). The “Berkeley Wedge”: an asymmetrical
10 energy-capturing floating breakwater of high performance. Marine Systems & Ocean
11 Technology, 9(1), 5-16.
- 12 [24]Chen, Q., Zang, J., Birchall, J., Ning, D., Zhao, X., & Gao, J. (2020). On the hydrodynamic
13 performance of a vertical pile-restrained WEC-type floating breakwater. Renewable Energy,
14 146, 414-425.
- 15 [25]Newman, J. N. (2018). Marine Hydrodynamics (p. 448). The MIT Press, Cambridge, Mass.
- 16 [26]Zheng, Y. H., You, Y. G., & Shen, Y. M. (2004). On the radiation and diffraction of water
17 waves by a rectangular buoy. Ocean engineering, 31(8-9), 1063-1082.
- 18 [27]Falnes, J. & Kurniawan, A. (2020). Ocean Waves and Oscillating Systems: Linear
19 Interactions Including Wave-Energy Extraction. Cambridge University Press, UK.
- 20 [28]Holthuijsen, L. H. (2010). Waves in Oceanic and Coastal Waters. Cambridge University
21 Press, UK.
- 22 [29]Sun, S. Y., Sun, S. L., & Wu, G. X. (2018). Fully nonlinear time domain analysis for
23 hydrodynamic performance of an oscillating wave surge converter. China Ocean
24 Engineering, 32(5), 582-592.
- 25 [30]Ren, J., Jin, P., Liu, Y., & Zang, J. (2021). Wave attenuation and focusing by a parabolic
26 arc float breakwater. Energy, 217, 119405.